

This item is the archived peer-reviewed author-version of:

Direct correlation of nanoscale morphology and device performance to study photocurrent generation in donor-enriched phases of polymer solar cells

Reference:

Ben Dkhil Sadok, Perkhun Pavlo, Luo Chieh, Mueller David, Alkarsifi Riva, Barulina Elena, Quiroz Yatzil Alejandra Avalos, Margeat Olivier, Dubas Stephan Thierry, Koganezawa Tomoyuki,- Direct correlation of nanoscale morphology and device performance to study photocurrent generation in donor-enriched phases of polymer solar cells

ACS applied materials and interfaces - ISSN 1944-8244 - 12:25(2020), p. 28404-28415

Full text (Publisher's DOI): <https://doi.org/10.1021/ACSAMI.0C05884>

To cite this reference: <https://hdl.handle.net/10067/1707030151162165141>

Direct correlation of nanoscale morphology and device performance to study photocurrent generation in donor enriched phases of polymer solar cells

Sadok Ben Dkhil, Pavlo Perkhun, Chieh Luo, David Müller, Riva Alkarsifi, Elena Barulina, Yatzil Alejandra AVALOS-QUIROZ, Olivier Margeat, Stephan Thierry Dubas, Tomoyuki Koganezawa, Daiki Kuzuhara, Noriyuki Yoshimoto, Claudia Caddeo, Alessandro Mattoni, Birger Zimmermann, Uli Würfel, Martin Pfannmöller, Sara Bals, Jorg Ackermann, and Christine Vidélot-Ackermann

ACS Appl. Mater. Interfaces, **Just Accepted Manuscript** • DOI: 10.1021/acsami.0c05884 • Publication Date (Web): 01 Jun 2020

Downloaded from pubs.acs.org on June 1, 2020

Just Accepted

“Just Accepted” manuscripts have been peer-reviewed and accepted for publication. They are posted online prior to technical editing, formatting for publication and author proofing. The American Chemical Society provides “Just Accepted” as a service to the research community to expedite the dissemination of scientific material as soon as possible after acceptance. “Just Accepted” manuscripts appear in full in PDF format accompanied by an HTML abstract. “Just Accepted” manuscripts have been fully peer reviewed, but should not be considered the official version of record. They are citable by the Digital Object Identifier (DOI®). “Just Accepted” is an optional service offered to authors. Therefore, the “Just Accepted” Web site may not include all articles that will be published in the journal. After a manuscript is technically edited and formatted, it will be removed from the “Just Accepted” Web site and published as an ASAP article. Note that technical editing may introduce minor changes to the manuscript text and/or graphics which could affect content, and all legal disclaimers and ethical guidelines that apply to the journal pertain. ACS cannot be held responsible for errors or consequences arising from the use of information contained in these “Just Accepted” manuscripts.

Direct correlation of nanoscale morphology and device performance to study photocurrent generation in donor enriched phases of polymer solar cells

Sadok Ben Dkhil,^{1,§} Pavlo Perkhun,¹ Chieh Luo,² David Müller,² Riva Alkarsifi,¹ Elena Barulina,^{1,3} Yatzil Alejandra Avalos Quiroz,¹ Olivier Margeat,¹ Stephan Thierry Dubas,^{4,5} Tomoyuki Koganezawa,⁶ Daiki Kuzuhara,⁷ Noriyuki Yoshimoto,⁷ Claudia Caddeo⁸, Alessandro Mattoni,⁸ Birger Zimmermann,² Uli Würfel,^{2,9} Martin Pfannmöller,^{10,#,} Sara Bals,¹⁰ Jörg Ackermann,¹ Christine Videlot-Ackermann^{1,*}*

¹ Aix Marseille Univ., UMR CNRS 7325, CINaM, 13288 Marseille, France.

² Fraunhofer Institute for Solar Energy Systems (ISE), Heidenhofstr. 2, 79110 Freiburg, Germany.

³ Dracula Technologies, 4 Rue Georges Auric, 26000 Valence, France.

⁴ The Petroleum and Petrochemical College, Chulalongkorn University, Bangkok 10330, Thailand.

⁵ Center of Excellence on Petrochemical and Materials Technology, Bangkok 10330, Thailand.

⁶ Industrial Application Division, Japan Synchrotron Radiation Research Institute (JASRI), Sayo, Hyogo 679-5198, Japan.

⁷ Department of Physical Science and Materials Engineering, Iwate University, Ueda Morioka 020 8551, Japan.

⁸ Istituto Officina dei Materiali (CNR-IOM), UOS Cagliari SLACS, Cittadella Universitaria, I-09042 Monserrato, Cagliari, Italy.

⁹ Materials Research Center FMF, University of Freiburg, Germany

1
2
3 ¹⁰ Electron Microscopy for Materials Research (EMAT), University of Antwerp,
4 Groenenborgerlaan 171, 2020 Antwerp, Belgium.
5
6
7
8
9
10
11
12

13 **KEYWORDS.** PTB7:PC₇₁BM, blend ratio, solar cell, additive, nanoscale fullerene network,
14
15
16 charge transport.
17
18
19
20
21
22

23 **ABSTRACT.** The nanoscale morphology of polymer blends is a key parameter to reach high
24 efficiency in bulk heterojunction solar cells. Thereby, research typically focuses on optimal
25 blend morphologies while studying non-optimized blends may give insight into blend design that
26
27 blend morphologies while studying non-optimized blends may give insight into blend design that
28 can be more robust against morphology defects. Here we focus on the direct correlation of
29 morphology and device performance of PTB7:PC₇₁BM bulk heterojunction (BHJ) blends
30 processed without additive in different donor:acceptor weight ratios. We show that while blends
31 of a 1:1.5 ratio are composed of large donor enriched and fullerene domains beyond exciton
32 diffusion length, reducing the ratio below 1:0.5 leads to blends composed purely of polymer
33 enriched domains. Importantly photocurrent density in such blends can reach values between 45
34 to 60% of those reached of fully optimized blend using additives. We provide here a direct visual
35 evidence that fullerenes in the donor enriched domains are not distributed homogeneously but
36 fluctuate locally. To this end, we performed compositional nanoscale morphology analysis of the
37 blend using spectroscopic imaging of low energy-loss electrons in the transmission electron
38 microscope. Charge transport measurement in combination with molecular dynamics simulations
39 show that the fullerene sub-structures inside the polymer phase generate efficient electron
40
41
42
43
44
45
46
47
48
49
50
51
52
53
54
55
56
57
58
59
60

1
2
3 transport in the polymer enriched phase. Furthermore, we show that the formation of densely
4 packed regions of fullerene inside the polymer phase is driven by the PTB7:PC₇₁BM enthalpy of
5 mixing. The occurrence of such a nanoscale network of fullerene clusters leads to a reduction of
6 electron trap states and thus efficient extraction of photocurrent inside the polymer domain.
7
8 Suitable tuning of the polymer acceptor interaction can thus introduce acceptor sub-networks in
9
10 polymer enriched phases improving the tolerance for high efficiency BHJ towards morphological
11 defects such as donor enriched domains exceeding exciton diffusion length.
12
13
14
15
16
17
18
19
20
21

22 **1. INTRODUCTION**

23
24
25

26 In the ongoing quest for efficient photon-to-electron conversion, polymer-based solar cells
27 (PSCs) have received an enormous amount of attention in renewable energy sources because of
28 their characteristics enabling solution processability, flexibility, large scale and low cost
29 production properties.¹⁻⁴ Recently, the development of novel non fullerene acceptors has allowed
30 to raise the power conversion efficiency (PCE) of PSCs to more than 18% in single junction
31 devices and 17% in tandem solar cells.⁵⁻⁷ Besides the rise of new acceptor materials, intensive
32 development on active layer structural optimizations, device engineering or morphology control
33 has contributed in obtaining these efficiencies.⁸⁻¹² The photo-active layer of high efficient solar
34 cells is prepared of a mixture of donor polymer and small molecule acceptor with a suitable
35 weight ratio defined as donor:acceptor (D:A) weight ratio leading to the formation of a
36 nanostructured bulk heterojunction (BHJ). To build a high-performance blend, several factors are
37 involved from materials to layers properties such as (i) a broad absorption overlap with the solar
38 spectrum, (ii) balanced and lossless charge transport, (iii) suitable bandgap and energy level
39 alignment between polymer and acceptor for charge separation and (iv) sufficient intermixing
40
41
42
43
44
45
46
47
48
49
50
51
52
53
54
55
56
57
58
59
60

1
2
3 between polymer and acceptor to ensure a bicontinuous network. Typically, it is assumed that the
4 optimization of the polymer blend morphology aims at the formation of a large D:A interface for
5 an efficient exciton dissociation in combination with a domain size equal to approximately twice
6 that of the exciton diffusion length.¹³ Parameters controlling nanoscale morphology of BHJs
7 have been addressed in several reviews.¹⁴⁻¹⁶ The D:A weight ratio in combination with the
8 molecular interaction and miscibility are the major driving forces. Solvent additives have been
9 found to further improve the nanoscale morphology of the blend.¹⁷ Although blend processing is
10 nowadays well understood,^{14,16} the optimization of a polymer blend is still delicate and specific
11 for each D:A couple. Particularly, large scale and thus industrial processing of organic solar cells
12 demand for photoactive materials that show a tolerance against non-optimized blend
13 morphologies to prevent performance loss. For example, the fabrication of polymer blend
14 containing morphological defects such large donor enriched domains with dimension surpassing
15 typical exciton diffusion length will lead to losses in device performance. Studying polymer
16 blends with such non optimal phase separation can provide precious information about concepts
17 of more robust blend materials that allow extracting electrons towards to acceptor enriched
18 domains without carrier recombination. In order to gain information about exciton dissociation
19 and charge carrier transport in such non-optimized polymer blends, visualization of the
20 nanoscale morphology and acceptor intercalation on polymer domains of BHJ is necessary.
21 Usually indirect measurements of domain size and acceptor intercalation can be applied to gain
22 insight into the nanoscale morphologies by combining real-space imaging techniques as atomic
23 force microscopy (AFM) and scanning electron microscopy (SEM) for surface information with
24 different XRD techniques.¹⁸⁻²³ There are only few examples of such a correlation of device
25 performance with direct visualization of, for instance, domain sizes or mixed phases.²⁴⁻²⁶ For
26
27
28
29
30
31
32
33
34
35
36
37
38
39
40
41
42
43
44
45
46
47
48
49
50
51
52
53
54
55
56
57
58
59
60

1
2
3 example, by applying nonlinear statistical analysis to variations in optical excitations measured
4
5 by electron spectroscopic imaging, varying phases, including mixed phase, can be localized at
6
7 the nanoscale in photoactive blends.²⁵ For localized analysis of compositional variations, the
8
9 near-edge structure in the X-ray absorption signal (NEXAFS) has been used in scanning
10
11 transmission X-ray microscopy.^{18,27} Unfortunately, the spatial resolution does not allow
12
13 visualization of domains or phases with features below 10 nm. On the other hand, spectroscopic
14
15 imaging of low energy-loss electrons in a transmission electron microscope (TEM) enable one to
16
17 directly correlate a specific nanoscale morphology with device performance.²⁸⁻²⁹ Furthermore
18
19 direct visualization of non-fullerene acceptors (NFAs) organization inside the polymer blends
20
21 has been recently demonstrated using analytic TEM.³⁰
22
23
24
25

26 In this work we focus on non-optimized polymer blends as a function of D:A weight ratio to
27
28 study photocurrent generation and nanoscale organization of acceptors in large polymer enriched
29
30 domains with domain sizes surpassing typical exciton diffusion lengths by applying
31
32 spectroscopic imaging with scanning transmission electron microscopy (STEM-SI) of the low
33
34 energy-loss for visualization. Although high efficiency polymer solar cells nowadays have
35
36 replaced fullerenes by NFAs, the manipulation of their nanoscale morphology is not so trivial
37
38 and well understood than in the case of fullerene based blends. Furthermore fullerenes are still
39
40 used in NFA based solar cells as third component in ternary blends making the choice of a
41
42 fullerene based model system relevant to study blends with morphological defects such as donor
43
44 enriched domains that are larger than corresponding exciton diffusion lengths.¹¹ For these
45
46 reasons, we select bulk heterojunctions comprising the donor polymer thieno[3,4-*b*]-thiophene-
47
48 *alt*-benzoditiophene (PTB7) and the fullerene acceptor [6,6]phenyl C₇₁ butyric acid methyl ester
49
50 (PC₇₁BM) (Figure 1a) as it allows to generate specific blend morphologies containing large
51
52
53
54
55
56
57
58
59
60

1
2
3 donor enriched domains.²⁹ The PTB7:PC₇₁BM blend is a well-known model system since cells
4 based on PTB7 blended with PC₇₁BM were the first cells to overcome a PCE of 7% in 2010 by
5 using chlorobenzene (CB) with 3% 1,8-diiodooctane (DIO) as solvents.¹³ Indeed it was shown
6 that solar cells using PTB7:PC₇₁BM blends yield performance improvement by using inverted
7 device structure,³¹ molecular weight (Mw) and polydispersity index (PDI) of PTB7,^{32,33} as well
8 as solvent additive,³⁴⁻³⁶ mixed solvent,^{18,37,38} and interface modification.^{39,40} Importantly the
9 device properties depend largely on the processing conditions with a particular control of the
10 photovoltaic performance by adding DIO to the blend solution.^{13,18,41,42} The use of DIO generates
11 a phase-separated structure composed of domain sizes of ~10 nm constituting a morphology
12 close to an ideal D:A nanometer-scale interpenetrating network.^{13,17,43} In contrast, PTB7:PC₇₁BM
13 blends using a weight ratio of 1:1.5 processed without DIO show a strongly non-optimized
14 nanoscale morphology composed of polymer enriched domains and large spherical fullerene
15 domains.²⁹ Importantly, DIO free-processed blends containing very large donor and acceptor
16 domains produce solar cells show relatively high photocurrent close to the 60% of cells with
17 optimal morphology.¹⁸ By comparing DIO-optimized PTB7:PC₇₁BM solar cells using a weight
18 ratio of 1:1.5 with DIO-free processed solar cells, Collins *et al.* concluded that the large polymer
19 enriched regions are inefficient for the charge separation due to high rate of germinate
20 recombination and therefore dead zones for the photovoltaic conversion.¹⁸ In a recent work, C.
21 Ho *et al.*⁴⁴ studied the early stage of D:A electronic interaction in PTB7:PC₇₁BM blends
22 processed with DIO demonstrating that electron trapping is the key limiting factor for BHJ solar
23 cells in the low fullerene content regime, while fast improvement in electron mobility was
24 observed for increase in fullerene concentration towards optimal regime. Hence, PTB7:PC₇₁BM
25 can be considered as an ideal model system allowing a large variety of blend morphologies
26
27
28
29
30
31
32
33
34
35
36
37
38
39
40
41
42
43
44
45
46
47
48
49
50
51
52
53
54
55
56
57
58
59
60

1
2
3 depending on the D:A ratio and use of DIO. To elucidate the reason for the large relative
4 photocurrent for DIO free cells, a direct visualization of the blends' nanoscale morphology in
5 correlation to device performance is essential.
6
7

8
9
10 To this end, we investigated the PTB7:PC₇₁BM BHJ system processed without additive via
11 varying the ratio of PTB7 and PC₇₁BM in the active layer (PTB7:PC₇₁BM at 1:1.5, 1:1, 1:0.5,
12 1:0.25). Optimized DIO-processes solar cells (with ratio 1:1.5) was used as a reference. The
13 ordering of both the polymer and fullerene was inspected via 2D grazing-incidence X-ray
14 diffractometry (2D-GIXD). To investigate the evolution of fullerene clusters and concentration
15 profiles at a resolution of better than 10 nm, the STEM-SI data was fitted to pure signals from
16 PTB7 and PC₇₁BM. We show that non-linearities through mixing, which were previously
17 determined by machine learning classification, do not hinder this concentration mapping.²⁵
18
19 Additionally transport studies were combined with molecular dynamics simulations of the
20 polymer-fullerene blends to understand transport properties and the enthalpy of mixing and
21 fullerene dispersion inside the blends. The combination of experimental evidence and simulation
22 reveals that in polymer-enriched phases with about 25% of fullerenes, sub-10 nm aggregates of
23 PC₇₁BM allow for efficient electron transport towards the fullerene enriched domains and hence
24 the observed high photocurrent. This behavior will support rationales on how the tolerance for
25 high efficiency BHJs towards non optimal blend morphologies can be enhanced.
26
27
28
29
30
31
32
33
34
35
36
37
38
39
40
41
42
43
44
45
46

47 **2. EXPERIMENTAL SECTION**

48
49
50
51 **2.1 Materials.** PTB7 was purchased from 1-Material and the fullerene derivative PC₇₁BM from
52 Nano-C (95% purity). The solvent additive 1,8-diiodoctane (DIO) was purchased from Sigma-
53 Aldrich (pb 167-169°C/6 mmHg(lit.)). ZnO nanocrystals were prepared as published
54
55
56
57
58
59
60

1
2
3 elsewhere.⁴⁵ Cluster free ZnO nanocrystal solutions in isopropanol (at 7.5 mg/mL) was prepared
4 by transferring the as-synthesized ZnO nanoparticles (6 nm as average diameter) from methanol
5 to isopropanol (IPA) mixed with ethanolamine (EA) at 0.2 wt%.

6
7
8
9
10 **2.2 Solar Cells Fabrication and Characterization.** Solar cells using regular device structures
11 were processed as detailed in former works.^{28,29} ITO substrates (purchased from Lumtec, 15
12 Ohm sq^{-1}) were thoroughly cleaned by sonication in acetone and ethanol followed by rinsing
13 with water and sonication in isopropanol and applying ultraviolet-ozone for 10 min. A thin layer
14 of poly(3,4-PEDOT:PSS) (CLEVIOSTM AI 4083) was spin-coated on the cleaned ITO pre-
15 coated glass substrate at the speed of 4000 rpm for 60 s followed by an annealing step on a hot-
16 plate at 140°C for 15 min leading to a thickness of 40 nm. The substrates were then transferred to
17 a nitrogen-filled glove box. PTB7:PC₇₁BM films with different weight ratios (1:0.25, 1:0.5, 1:1
18 and 1:1.5) were prepared in nitrogen-filled glove box by fixing the PTB7 amount (10 mg/mL)
19 and varying the PC₇₁BM content (2.5, 5, 10 and 15 mg/mL). The spin-coating was done at
20 ambient temperature (21-25°C) in glove box. The DIO-processed PTB7:PC₇₁BM solution at a
21 weight ratio of 1:1.5 was prepared by mixing solvents chlorobenzene/1,8-diiodoctane with
22 97:3% by volume. The DIO-free PTB7:PC₇₁BM solutions were prepared by using chlorobenzene
23 as solvent. Finally, an overnight stirring at 65°C was employed to finalize the ready-to-use
24 PTB7:PC₇₁BM blend solutions for the spin-coating solution process. The different solutions were
25 spin-coated with controlled speeds to obtain thin films with equal thickness of 90±5 nm (ratio
26 1:1.5 at rpm = 1800, ratio 1:1 at rpm = 1500, ratio 1:0.5 at rpm = 1200, ratio 1:0.25 at rpm =
27 1100 and ratio 1:0 at rpm = 1000). The spin coating time was fixed at 120 sec. After dried in
28 vacuum overnight, ZnO-based ILs were deposited by spin-coating ZnO nanocrystal solution on
29 top of active layers at 1500 rpm for 60 s followed by annealing for 5 min at 80°C; all processes
30
31
32
33
34
35
36
37
38
39
40
41
42
43
44
45
46
47
48
49
50
51
52
53
54
55
56
57
58
59
60

1
2
3 were done inside the glove box. To complete the device, aluminum (Al) metal electrodes were
4 thermally evaporated (MBRAUN evaporator) at 2×10^{-6} Torr to a thickness of 100 nm using a
5 shadow mask that define the device area of the solar cells to 0.27 cm^2 .
6
7
8
9

10
11 The current density–voltage (J-V) characteristics of the solar cells were measured inside the
12 glove box using a Keithley 238 Source Measure Unit and a Newport class AAA 1.5 Global solar
13 simulator (Oriel Sol3ATM model n° 94043A) with an irradiation intensity of 100 mW/cm^2 . The
14 light intensity was determined with a Si reference cell (Newport Company, Oriel n° 94043A)
15 calibrated by National Renewable Energy Laboratory (NREL). Spectral mismatch factors (M)
16 were calculated according to a standard procedure and a typical M value of 1.02 was obtained for
17 the PTB7:PC₇₁BM devices.⁴⁵ The value was used to correct the measured J_{sc} values of the solar
18 cells to J_{sc} values corresponding to AM1.5G conditions. Shadow masks were used to well-define
19 the illuminated area to $0.27 \times 1.0 \text{ cm}^2$. We present the performance of the best devices, whereas
20 average PCEs were obtained with a standard deviation analysis calculated using 6-9 devices.
21
22
23
24
25
26
27
28
29
30
31
32
33

34 External quantum efficiency (EQE) measurements were performed in air using a homemade
35 setup consisting of a Keithley 238 Source Measure Unit and Newport monochromator. Light
36 intensity was measured with a calibrated Si-diode from Newport.
37
38
39
40

41 **2.3 Thin film Characterizations.** UV-Vis absorption spectra of PTB7, PC₇₁BM and blend
42 layers were recorded using a Varian CARY 5000 spectrophotometer.
43
44
45
46

47 Polymer blends were further analyzed by 2D grazing-incidence X-ray diffractometry (2D-GIXD)
48 with high-brightness synchrotron radiation at BL19B2 in SPring-8. 2D-GIXD measurements
49 were performed using a high-sensitive 2D X-ray detector (PILATUS 300K). The incident angle
50 and wavelength of X-rays were 0.13° and 0.100 nm , respectively.
51
52
53
54
55
56
57
58
59
60

STEM-SI measurements were performed at 120 kV using a Titan 60–300 microscope (ThermoFisher Scientific, USA) and an Enfinium spectrometer (Gatan/ThermoFisher Scientific, USA). Planar specimens were prepared by floating the photoactive layer onto water and capturing with a holey carbon film (QUANTIFOIL®) on an electron microscopy grid. To visualize potential small domains in blends of donor:acceptor ratios of 1:0.25 and 1:0.5, layer thicknesses of ca. 50 nm were used whilst for higher fullerene concentrations with large agglomerates layers with thickness of about 70 nm were investigated. In a previous work, we qualitatively investigated the nanoscale morphology of PTB7:PC₇₁BM blends with a thickness of 90 nm with and without DIO.²⁹ Despite the different perspective and only qualitative nature, the general nanoscale morphologies for the ratio 1:1.5 are identical when comparing layers of 90 and 70 nm thickness. Therefore, we expect that further reduction to a thickness of 50 nm through higher spin-coating speed and thus faster drying time does not compromise the validity of the morphological analyses in the current work. The lamella and micro-pillar samples were prepared from solar cell devices with a Helios Nanolab 650 (ThermoFisher Scientific, USA). Scanning step sizes for STEM-SI imaging were set to 3 nm for planar analyses, and to 2 nm for cross-sectional analyses and for the higher resolution map of the 1:0.5 ratio sample in Figure S9. Spectroscopic imaging (SI) data sets were processed using HyperSpy.⁴⁶ To use single scattering spectra and account for thickness variations, all spectra of a data set were processed by Fourier-log deconvolution. Multiple linear least-squares fitting was performed by a custom Python script using the LMFIT package.⁴⁷ As outlined in the supporting information in Table S1 and Figure S8, for theoretical concentrations of different nominal mixing ratios, weight ratios were transformed into (mono-)molecular ratios using molecular weights of PC₇₁BM molecules and PTB7 monomers.

1
2
3 **2.4 Space Charge Limited Current device Fabrication and Measurements.** Space Charge
4 Limited Current (SCLC) devices require careful choice of the contacts to ensure sufficient
5 injection of the desired carrier, and effective blocking of the other carrier to work like single-
6 carrier devices. Hole-only and electron-only devices consisted of
7 ITO/PEDOT:PSS/PTB7:PC₇₁BM/MoO_x/Au and ITO/ZnO/PTB7:PC₇₁BM/LiF/Al, respectively.
8 ZnO was purchased from Avantama. Top metallic electrodes were thermally evaporated
9 (MBRAUN evaporator) at 2×10⁻⁶ Torr to a controlled thickness (13 nm of MoO_x, 100 nm Au,
10 0.5 nm LiF and 100 nm of Al) using a shadow mask that define the device area to 0.09 cm² and
11 allowed a four-point measurement. The pristine PTB7:PC₇₁BM solutions were deposited by spin-
12 coating at speeds ranging from 600 to 2500 rpm for 120 sec. Active layers were subsequently
13 annealed at 80°C during 5 minutes. The thickness of thin films deposited on glass substrate was
14 measured with a Veeco Dektak 150 (Table S2).

15
16
17
18
19
20
21
22
23
24
25
26
27
28
29
30
31
32 The measured dark current was fitted using the Murgatroyd expression:

$$I = A\mu_0 \frac{9V^2}{8d^3} \epsilon\epsilon_0 \exp(0.891\gamma\sqrt{\frac{V}{d}}) \quad (\text{eq. 1})$$

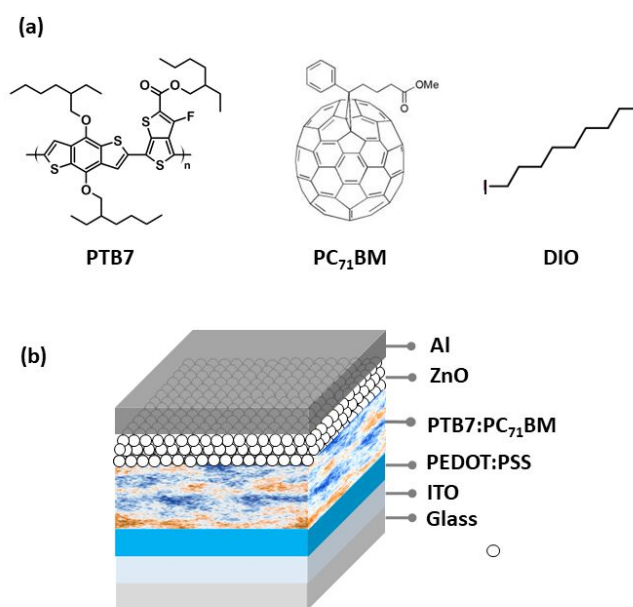
33
34
35
36
37 where d is the active layer thickness, A is the active device area, $\epsilon\epsilon_0$ is the permittivity of the
38 active layer (ϵ is assumed equal to 3.5 and ϵ_0 is the permittivity of free space), and V is the
39 voltage. μ_0 and γ are the unknown parameters that will be adjusted to get a good fit, all other
40 parameters are fixed. μ_0 is the mobility at low electric fields, and γ is a parameter that represents
41 the field dependence of mobility. Measurements and analysis of I-V curves were made following
42 a specific previously reported protocol.⁴⁸ A complete worked example and the corresponding
43 data fitting (Figures S10-S12) is given in the supporting information.
44
45
46
47
48
49
50
51
52
53
54
55
56
57
58
59
60

1
2
3 **2.5 Molecular Dynamics Methods.** The PTB7 polymer and PC₇₁BM fullerene derivative have
4 been modeled using the General Amber Force Field (GAFF),⁴⁹ which has been successfully
5 adopted to describe fully organic as well as hybrid organic-inorganic blends.⁵⁰⁻⁵³ The atomic
6 partial charges were calculated according to the standard AM1-BCC method and the dispersive
7 (i.e., van der Waals) interactions (both intra- and intermolecular) were described by the sum of
8 two-body Lennard–Jones contributions, with Amber force field parameters.⁴⁹ Model potential
9 molecular dynamics simulations were performed by using the NAMD 2.0 molecular simulations
10 package.⁵⁴ The equations of motion of atoms were integrated by using the Velocity Verlet
11 algorithm with a time step as small as 1.0 fs. Multiple time stepping was used, with short-range
12 nonbonded interactions calculated every two time steps and full electrostatics evaluated every
13 four time steps. All the electrostatic contributions were computed by the Particle Mesh Ewald
14 (PME) sum method, with grid spacing of 1 Å. Temperature was controlled by Langevin
15 thermostat with damping coefficient of 1 ps⁻¹. Rigid bonds conditions were applied for the
16 hydrogens and the atoms to which they are bonded. The VMD 1.9 molecular visualization
17 program has been used to analyze the trajectories.^{55,56} The PTB7 bulk consists of 20 regioregular
18 PTB7 chains of length \approx 12 nm and periodically replicated along the backbone to mimic an
19 infinite chain. Equilibration at room temperature and pressure was obtained by annealing using
20 the Langevin thermostat and barostat (constant pressure constant temperature NPT ensemble)
21 with anisotropic cell fluctuations for 1 ns. The fullerene bulks were composed by 32 molecules
22 and built accordingly to the conformation described in Casalegno *et al.* for both species, and
23 relaxed with the same procedure used for PTB7.⁵⁷⁻⁵⁹ The cohesive energy density (CED) has
24 been calculated by subtracting the energy of the isolated molecules from those of the relaxed
25 systems and dividing by the equilibrated volume.

3. RESULTS AND DISCUSSION

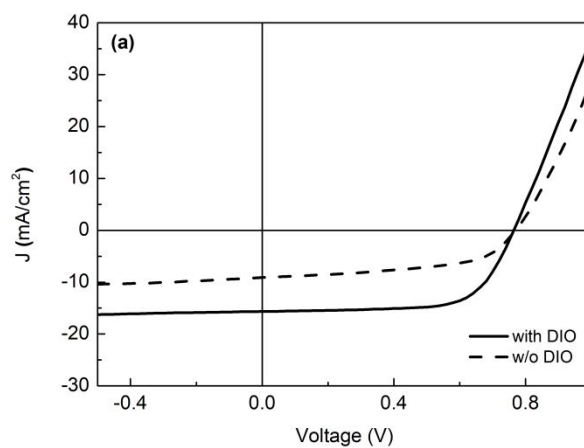
3.1 Comparison DIO-free and DIO processed solar cells

We first investigated solar cells prepared with PTB7 as electron donor mixed with PC₇₁BM as electron acceptor at the PTB7:PC₇₁BM weight ratio of 1:1.5 using either DIO as solvent additive or pure chlorobenzene solution. A schematic of the device structure explored is shown in Figure 1b. The current density-voltage (J-V) curves under solar illumination and the corresponding external quantum efficiency (EQE) spectra are displayed in Figure 2a and 2b, respectively. DIO as a commonly used high boiling point additive significantly improves device performance as previously reported.^{13,42} Resulting photovoltaic parameters (power conversion efficiency PCE, open-circuit voltage V_{oc} , short-circuit density J_{sc} and fill factor FF) are higher for the DIO-processed devices as highlighted in Table 1. PCE is more than doubled from 3.6% to 8%, which is caused by an increase in FF and J_{sc} . EQE values improve drastically with the addition of DIO to attain a maximum of 70% for the DIO-containing active layer. Nevertheless, the EQE spectra of both devices show a quasi-identical profile of photoconversion efficiency in the whole range from 300 to 800 nm corresponding to the resulting absorption of PTB7:PC₇₁BM blend films (see Figure S1). This indicates that in both cases PC₇₁BM and PTB7 contribute identically to the photocurrent generation.



26
27
28
29
30

Figure 1. (a) Chemical structures of PTB7, PC₇₁BM and DIO and (b) Schematic multi-layer device structure of bulk heterojunction solar cells.



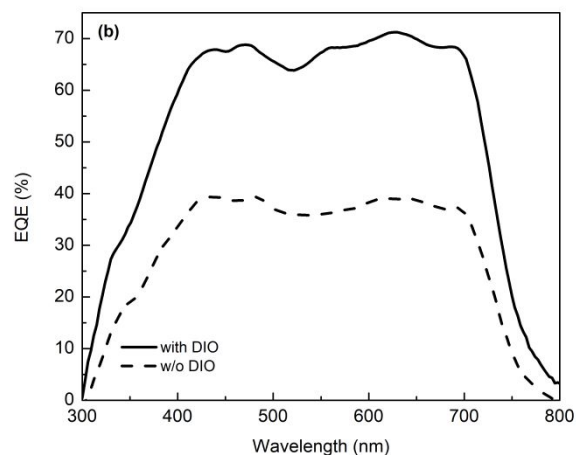


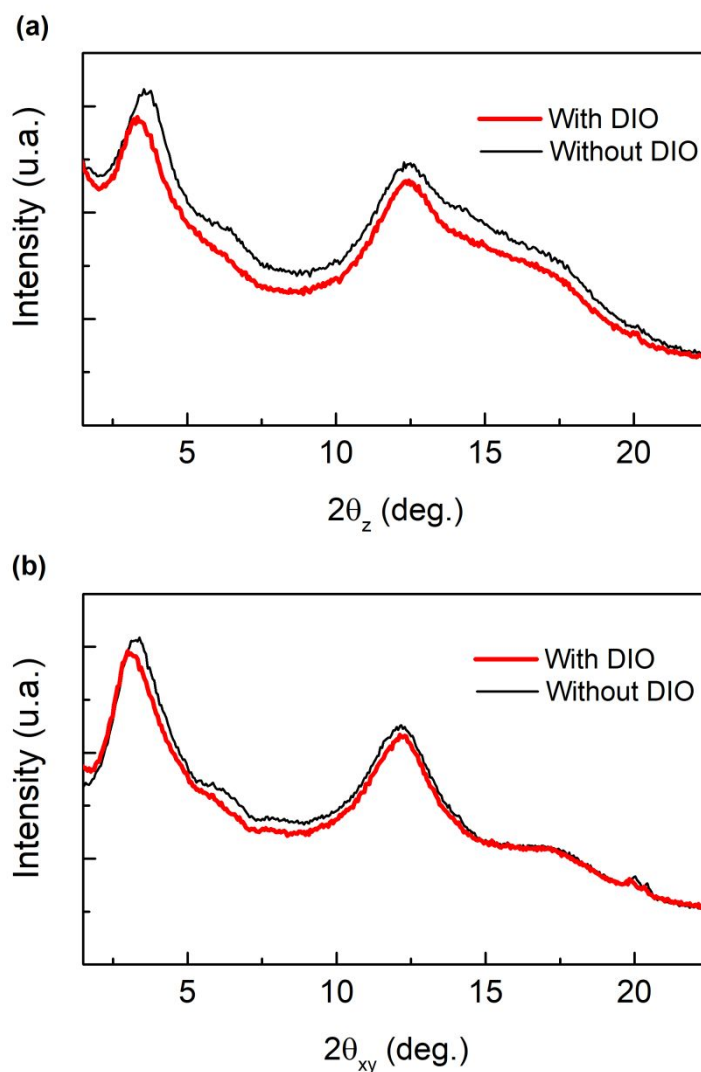
Figure 2. J-V curves (a) and EQE spectra (b) of PTB7:PC₇₁BM solar cells (blend ratio 1:1.5) processed with and without DIO.

Table 1. Photovoltaic parameters (PCE, V_{oc} , J_{sc} and FF) of PTB7:PC₇₁BM bulk heterojunction solar cells as function of solvent additive DIO and blend ratio.

| | PTB7:PC ₇₁ BM ratio | PCE (%) | V_{oc} (V) | J_{sc} (mA/cm ²) | FF (%) | average PCE (\pm std dev.) |
|-------------|--------------------------------|---------|--------------|--------------------------------|--------|-------------------------------|
| with DIO | 1:1.5 | 8 | 0.764 | 15.64 | 67 | 7.89 \pm 0.09 |
| without DIO | 1:1.5 | 3.6 | 0.77 | 9.05 | 52.3 | 3.44 \pm 0.11 |
| | 1:1 | 3.6 | 0.78 | 9.37 | 49.4 | 3.39 \pm 0.13 |
| | 1:0.5 | 2.95 | 0.80 | 8.23 | 44.9 | 2.75 \pm 0.18 |
| | 1:0.25 | 1.86 | 0.735 | 7.05 | 36 | 1.65 \pm 0.14 |
| | 1:0 | 0.86 | 0.558 | 5.01 | 31 | 0.63 \pm 0.20 |

In Figure 3 we compare the out-of-plane and in-plane GIXD profiles of PTB7:PC₇₁BM blend films at ratio 1:1.5 with and without DIO. The corresponding 2D-patterns as well as from pure donor and acceptor layers are provided in Figures S2 and S3, respectively. The profiles overlap nearly perfectly and reflect additive behavior of PC₇₁BM and PTB7 peaks (Figure S4 and S5) for

1
2
3 the parts corresponding to scattering angles superior to 5 deg. However, the peak in the range of
4 small scattering angle (at 2.5-5 deg.) corresponding to the lamellar spacing of PTB7 polymer
5 chains shifted in position to smaller angles when DIO was used indicating that the packing
6 distance between lamellar polymer increased due to the addition of fullerenes in the polymer
7 matrix.^{18,44,60}
8
9
10
11
12
13
14
15
16



53 **Figure 3.** 2D-GIXD profiles of blend PTB7:PC₇₁BM films (ratio1:1.5) processed with and
54 without DIO: (a) out of plane (z) of line cut and (b) in plane (xy) of line cut.
55
56
57
58
59
60

1
2
3
4
5 2D-GIXD does not provide information on local domain and interface distribution. Therefore we
6 applied STEM-SI in the low-energy-loss range to visualize nanoscale textures in neat and DIO-
7 processed blends. The technique allows recording spatially resolved spectra of optical excitations
8 and thereby enables distinguishing between donor and acceptor phases of blends similar to
9 energy-filtered imaging series.^{24,61} To create morphological maps, we used plasmon peak
10 positions as mapped feature or machine learning on a spectral data set. The latter revealed minute
11 non-linear effects between pure and mixed phases.²⁵ However, to a first approximation spectral
12 signals of mixed regions can be approximated by linear combinations of spectra from pure donor
13 and acceptor layers. Here, we use signals from PTB7 and PC₇₁BM pure layers (see Figure S6) to
14 determine the spatial composition variations - and thereby also domain distributions - by
15 multiple linear least-squares fitting to STEM-SI data sets of blends. In the fitting procedure the
16 composite spectra from the blends are treated as linear combinations of the pure spectra.
17 Mapping the determined coefficient for the fullerene spectrum in the linear combinations reveals
18 the compositional distribution. In Figure 4, we compare conventional annular dark-field STEM
19 images (Figures 4a and 4b) and maps of fullerene concentrations from fitting of STEM-STI data
20 of neat and DIO-processed PTB7:PC₇₁BM blend layers (Figures 4c and 4d). The nanoscale
21 materials phases are identified as PC₇₁BM rich domains in brown and PTB7 rich domains in blue
22 together with the mixed phase in white. Comparing the morphologies of the DIO-processed
23 blend with the blend processed without DIO reveals the expected differences with much finer
24 details induced by additive use.²⁹ As previously reported, DIO selectively dissolves PC₇₁BM
25 aggregates, thereby providing efficient intermixing between donor and acceptor molecules where
26 PC₇₁BM intercalates into PTB7 backbones optimizing both the domain size and the D:A
27
28
29
30
31
32
33
34
35
36
37
38
39
40
41
42
43
44
45
46
47
48
49
50
51
52
53
54
55
56
57
58
59
60

1
2
3 interface.⁶² Importantly, the compositional maps allow profiling of fullerene concentration.
4
5 Figure 4e shows two averaged line profiles from the two given maps. For the D:A ratio of 1:1.5
6
7 and when using DIO, the domain sizes of both donor and acceptor enriched phases are small
8
9 within a size range of 5-20 nm, which conforms with exciton diffusion lengths.⁶³⁻⁶⁵ It is thus
10
11 likely that excitons photogenerated inside PTB7 and PC₇₁BM diffuse to the D:A interface, i.e.
12
13 the mixed phase, which is present at high percentage (about 38% of phases as shown in a
14
15 previous work)²⁹. In contrast, without additive large fullerene agglomerates form surrounded by
16
17 polymer enriched phases, with domain sizes of > 100 nm, which is significantly larger than
18
19 exciton diffusion lengths.
20
21
22
23
24
25
26
27
28
29
30
31
32
33
34
35
36
37
38
39
40
41
42
43
44
45
46
47
48
49
50
51
52
53
54
55
56
57
58
59
60

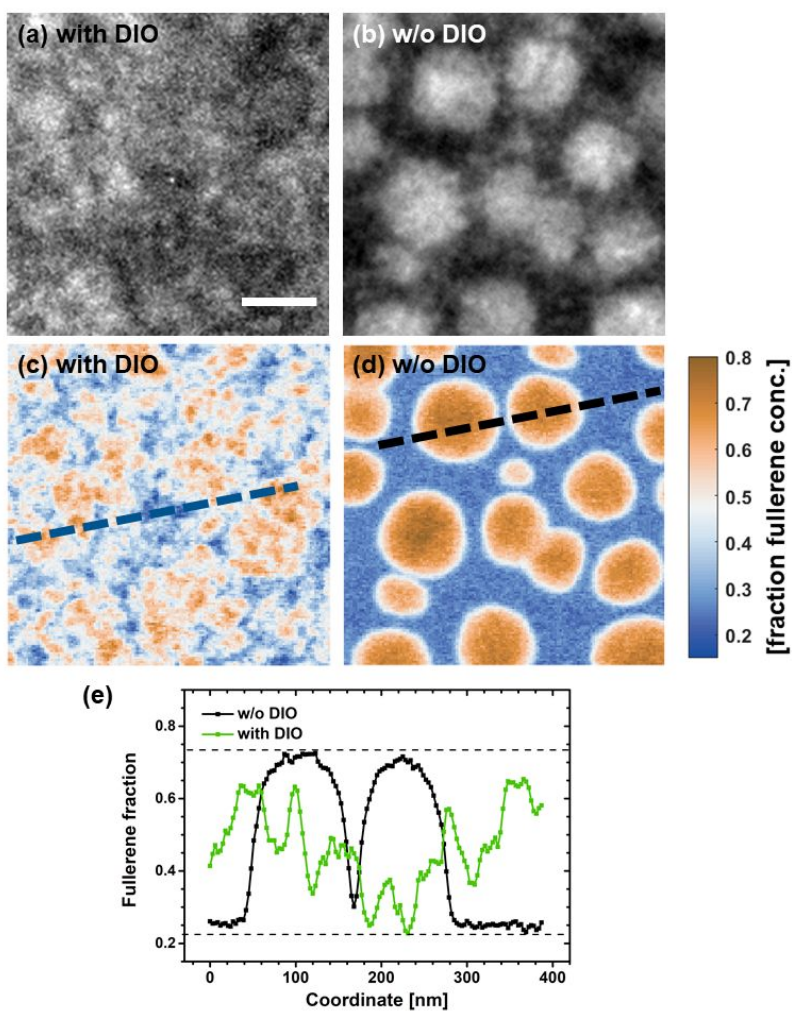


Figure 4. Annular dark-field STEM micrographs (a,b) and STEM-SI concentration maps of the fullerene fraction (c,d) of PTB7:PC₇₁BM blends (ratio 1:1.5) processed with DIO (a,c) and without DIO (b,d). The minimum value of the colourmap encoding the fullerene concentration ratio was set to 0.16 to highlight the fullerene concentration ratio of about 0.25 in the polymer enriched phase of the DIO free blend. Scale bar: 100 nm. (e) Line profiles of fullerene fraction in STEM-SI maps.

Interestingly, the composition profiles for both layers show a minimum fullerene concentration of about 23%. To show that this is not a result from overlapping domains and additive signal

1
2
3 projection in the STEM experiment we generated dark-field and compositional maps of cross-
4 sectional views (Figure S7). DIO-processed blends show a uniform bulk distribution of the three
5 coexisting phases (PC₇₁BM rich phase, the PTB7 rich and mixed phase). The thickness profile
6 for the blend without DIO would show a continuous polymer enriched layer with 23% fullerene
7 concentration. This implies that concentration variations around 23% are not due to overlapping
8 domains. The enriched PTB7 phase in direct contact with the mixed phase surrounding the
9 acceptor domain acts as a continuous active layer sandwiched between the anode and the
10 cathode. Simultaneously, the fullerene agglomerate concentration mapped in Figure 4d can be a
11 result of overlapping. The large fullerene agglomerate in Figure S7d is found on top of the small
12 polymer-enriched layer. Hence, the maximum fullerene concentration in fullerene agglomerates
13 must be larger than 73% as determined in projection through the layer (Figure 4d-e). Although
14 the device performance decreases when no DIO is used, a significant J_{sc} is observed (see Figure
15 2a). Thus, the direct observation of the nanoscale morphology of DIO-free films shows that
16 photocurrent generation may be a complex process in such layers, which are composed of large
17 fullerene domains wrapped by the polymer-enriched phase. Indeed we can expect that the donor
18 phase should actively contribute to the photocurrent generation, but it is an open question to what
19 extent compared to the fullerene domains. The fullerene concentration in the PTB7 enriched
20 phase has been determined to be about 25% (see Figure 4e) corresponding to the maximum
21 miscibility of PC₇₁BM in PTB7 as reported in the literature.²⁹ This fullerene concentration may
22 enable the formation of a bicontinuous network along the BHJ inside the donor phase. In order to
23 answer these questions, we chose to characterize PTB7:PC₇₁BM based solar cells with lower
24 acceptor concentration to study blends only composed of a polymer enriched phase.
25
26
27
28
29
30
31
32
33
34
35
36
37
38
39
40
41
42
43
44
45
46
47
48
49
50
51
52
53
54
55
56
57
58
59
60

3.2 Photocurrent generation in polymer enriched blend solar cells

We varied the mass ratio of PTB7 and PC₇₁BM in the active layer using 1:1.5, 1:1, 1:0.5, and 1:0.25 and determined the fullerene concentration maps from spectroscopic imaging data sets. To show that the determined concentration maps and average concentration measures are valid using the spectral fitting procedure, we compared experimentally with theoretically expected values (Figure S8 and Table S1). Since the spectral composition is rather related to the number of molecules than the mass fraction in the layer, we converted the mass ratios to molecular ratios (see Experimental part and Table S1). Resulting D:A molecular ratios are 0.48:0.52, 0.58:0.42, 0.73:0.27, 0.85:0.15. We kept these numbers without scaling to highlight that for a mass ratio of 1:0.5, a molecular ratio of 0.73:0.27 is obtained, i.e. with 27% fullerenes a concentration where increased agglomeration should commence. In Figure S8 we provide experimentally determined molecular ratios as averages from three data sets for each of the four blends. Although at high fullerene concentration we observe an increasing underestimation of the fullerene content, the values are very close to the theoretical ones with a maximum deviation of 8%. Figure 5 shows annular dark-field images (Figure 5a-e) and corresponding concentration maps (Figure 5f-j) for all indicated mass ratios. The pure polymer layer (Figure 5e and 5j) is shown as reference. From D:A ratio of 1:1.5 (Figures 5a and 5f) to 1:1 (Figures 5b and 5g), several morphological aspects of the layer change. The diameter of the fullerene domains decreases leading to an enlargement of their separation distance, i.e. an increase of the PTB7-enriched phase. For the ratio of 1:0.5 (Figures 5c and 5h), the large fullerene domains disappear to leave alone the polymer-enriched phase. However, the concentration map shows a color contrast in this phase of very small nano-sized structures with fullerene concentration up to about 0.5. This implies that whereas the average fullerene concentration ratio in the layer is about 0.27 (see Table S1), small fullerene

1
2
3 aggregates of a concentration ratio approaching 1 are embedded in the polymer matrix. A higher
4 resolution map showing the variable concentrations or domains at the nanometer level is
5 provided in Figure S9. Further decrease in fullerene concentration to a ratio of 1:0.25 (Figures 5d
6 and 5i) leads to homogeneous layers in which the fullerene concentration is clearly reduced, and
7 the nano-sized structures are not visible anymore. The concentration map resembles the map for
8 the pure polymer layer. Nevertheless, the average molecular fullerene fraction for this sample is
9 determined to be 0.15. Due to the required large dynamic range, the colourmap cannot display
10 the fine variations in this range of concentrations. By comparing the layers with high fullerene
11 concentration in both top view as well as cross view (Figure S7) with the layer of ratio 1:0.5, we
12 observe similar fullerene sub-structures in the polymer enriched domains for the 1:1 and 1:1.5
13 ratios (see Figures 5f and 5g). Only below 1:0.5, no sub-structures are observed in the polymer
14 enriched phase. We note that here, very small agglomerations < 4 nm (the nominal resolution in
15 Figure S9) might exist and indeed not be detected due to overlapping effects. The observation of
16 sub-structures indicates that fullerenes are not homogeneously distributed inside the polymer but
17 reorganized into clusters of local concentrations larger than 23-27%, i.e. clearly more than the
18 maximum miscibility of PC₇₁BM in PTB7, surrounded by polymer domains with local
19 concentrations of less than 23% (see Figure S9).
20
21
22
23
24
25
26
27
28
29
30
31
32
33
34
35
36
37
38
39
40
41
42
43
44
45
46
47
48
49
50
51
52
53
54
55
56
57
58
59
60

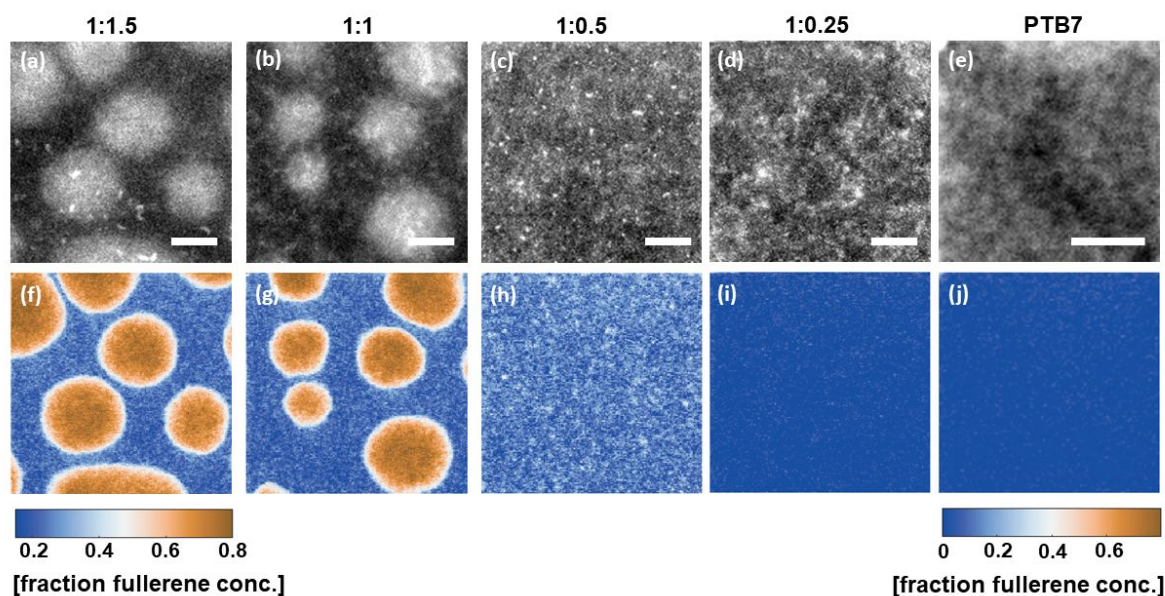


Figure 5. Annular dark-field STEM micrographs (a-e) and STEM-SI concentration maps of fullerene fractions (f-j) of PTB7:PC₇₁BM blends processed without DIO as blend ratio: ratio 1:1.5 (a, f), 1:1 (b, g), 1:0.5 (c, h) and 1:0.25 (d, i) while 1:0 corresponds to PTB7 (e,j). Scale bar: 100 nm.

The J-V characteristic curves and EQE spectra of the solar cells processed with the corresponding blends are shown in Figure 6a and 6b, respectively. The photovoltaic performances are summarized according to the J-V curves and listed in Table 1. With a FF comparable to the pure PTB7 device (31-36%), the D:A weight ratio 1:0.25 suffers mainly from the small amount of fullerene where a low average PCE value of 1.65% is obtained. With comparable J_{sc} (8.23-9.08 mA/cm²) and FF (45-52%), the D:A weight ratios 1:1.5 to 1:0.5 suggest a charge generation that is with low dependence of D:A ratio. Furthermore, PCE is decreased by less than 20% when the ratio is reduced from 1:1.5 to 1:0.5.

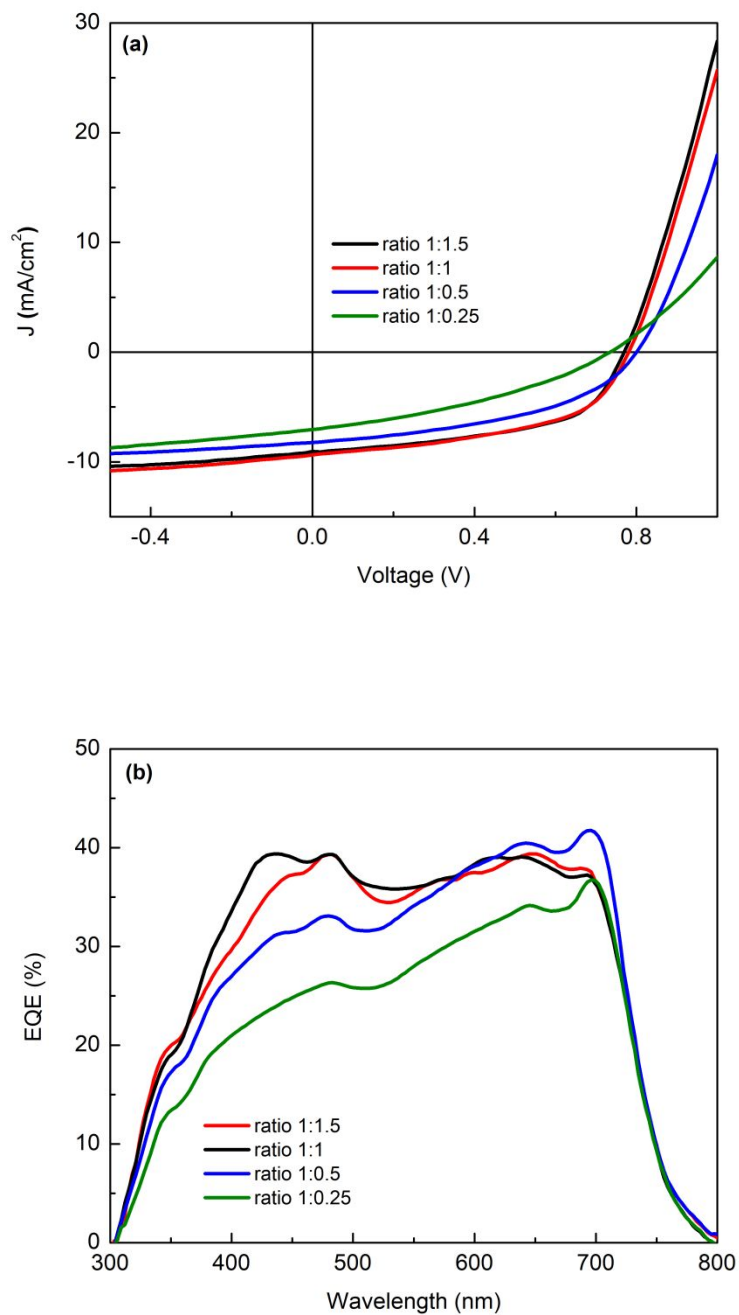


Figure 6. J-V curves (a) and EQE spectra (b) of PTB7:PC₇₁BM solar cells processed without DIO and with blend ratio 1:0.25, 1:0.5, 1:1 and 1:1.5.

1
2
3 By using the equation (eq 2), thus neglecting recombination:
4
5

$$6 \quad G = \frac{J}{ed} \quad (\text{eq. 2})$$

7
8
9

10 where J is the measured current density under reverse bias (-0.5 V), e is the elementary charge
11 and d the thickness of thin films, the generation rates are calculated as $0.6\text{-}0.74 \times 10^{28} \text{ m}^{-3}\text{s}^{-1}$ for
12 the DIO-free processed active layers of ratio 1:1.5 and 1:0.5, respectively.⁴¹ The comparable
13 generation rate implies the same D:A interface for exciton splitting and thus identify the polymer
14 enriched phase with the fullerene sub-structure to be strongly involved in the photocurrent
15 generation. Taking into account the EQE spectra (Figure 6b) both polymer and fullerene
16 contribute equally to the photocurrent generation independently of ratio 1:1.5, 1:1: and 1:0.5 with
17 only a small decrease in the range of 400-550 nm related to the reduction of the fullerene
18 concentration and thus absorption. Regarding the J-V characteristics for the 1:0.5 ratio together
19 with the nanoscale morphology visualization (Figure 5h), we can thus clearly say that a large part
20 of the photocurrent density can be generated in polymer enriched phase with values of more than
21 60% of the J_{sc} obtained in DIO-processed and optimized solar cells. Moreover, our observations
22 show that the interface of exciton dissociation does not solely occur at the interface between the
23 large donor and polymer enriched domains, which are present with ratios 1:1.5 and 1:1. Excitons
24 are thus dissociated throughout the donor enriched phase at the interface with the fullerene sub-
25 structures while electrons are likely to be transported across sub-structures towards the fullerene
26 enriched domains.
27
28
29
30
31
32
33
34
35
36
37
38
39
40
41
42
43
44
45
46
47
48
49

50 To understand the mechanism of the photocurrent transport inside polymer enriched phase
51 containing the fullerene sub-structure, 2D-GIXD measurements can be analyzed with respect to
52 the incorporation of the fullerenes inside the polymer. The predominant composition of PTB7 is
53
54
55
56
57

1
2
3 confirmed by 2D-GIXD on DIO-free processed PTB7:PC₇₁BM active layer systems (see Figure
4 S5) where the intensities of the PTB7 reflections are highly underlined in the profile of D:A layer
5
6
7 at 1:0.5 with a main peak at $2\Theta_z$ of 14.8 deg. Nevertheless, the incorporation of fullerene in the
8
9
10 polymer network is also highlighted by the presence of shoulders at $2\Theta_z$ of 12.5 and 17.7 deg.
11
12 corresponding to the peak of bare PC₇₁BM. This proves that the nano-sized structures in Figure
13
14
15 5h correspond to the small PC₇₁BM domains with a crystalline organization making charge
16
17 transport efficient between the fullerenes. It was shown for DIO-processed PTB7:PC₇₁BM active
18
19 layer systems, reported by Ho *et al.*, that fullerene domains should act as small nanoparticles
20
21 responsible of the electron conduction once the fullerene concentration reaches the percolation
22
23 threshold of more than 1:0.3.⁴⁴ To evaluate the impact of the formation of the fullerene sub-
24
25 structures in the case of DIO-free processed layers, we determined the charge transport
26
27 properties of the blend films with different D:A weight ratio. To this end we used the SCLC
28
29 protocol described by Blakesley *et al.*⁴⁸ extracting the mobility from I-V curves of hole-only
30
31 devices and electron-only devices. I-V curves were fitted using equation (1) in the SCLC region
32
33 considering a field-dependence of the mobility. Hole (μ_h) and electron (μ_e) mobility values
34
35 obtained for PTB7:PC₇₁BM BHJ layers without DIO as function of blend ratio are summarized
36
37 in Table 2. A complete worked example and the corresponding data fitting is given in SI together
38
39 with the values of thicknesses in Table S2. Figure 7 shows representative dark current and fitting
40
41 curves for each blend ratio. Based on hole-only devices, the hole mobility is not reduced by
42
43 blending with PC₇₁BM with a value consistent with the hole mobility of neat PTB7 obtained
44
45 previously by SCLC.^{13,44,66-68} In contrast, the electron mobility in PTB7:PC₇₁BM blends is
46
47 largely impacted as function of PC₇₁BM content. For both 1:1.5 and 1:1, the electron mobility
48
49 reaches the saturated values of $1-6 \times 10^{-4}$ cm²/Vs to be consistent with the reported values.⁴⁴ Well
50
51
52
53
54
55
56
57
58
59
60

balanced electron and hole mobilities were obtained at 1:1.5 and 1:1 ratio, together with higher PCE and FF restricting the build-up of space charges, and hence, reducing charge recombination. At the D:A ratio of 1:0.5, the electron mobility decreases but does not completely diminish with values of $3.8\text{-}8.6 \times 10^{-6} \text{ cm}^2/\text{Vs}$, which are close to mobilities observed in DIO processed blends at identical ratio. This indicates that the electron transport pathway persists in percolation through the crystalline small domains observed in thin films by STEM-SI and 2D-GIXD.

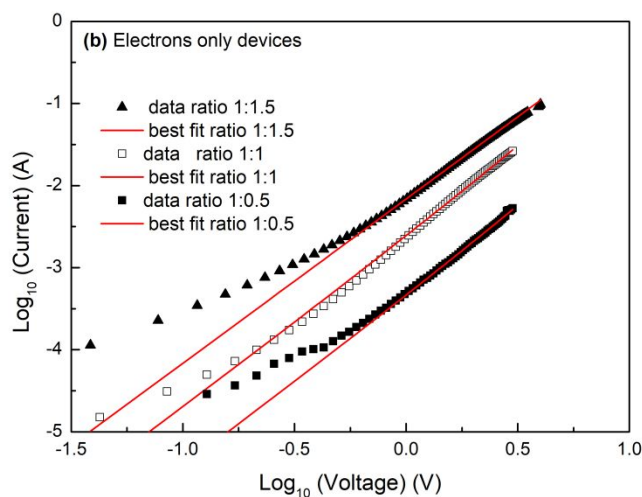
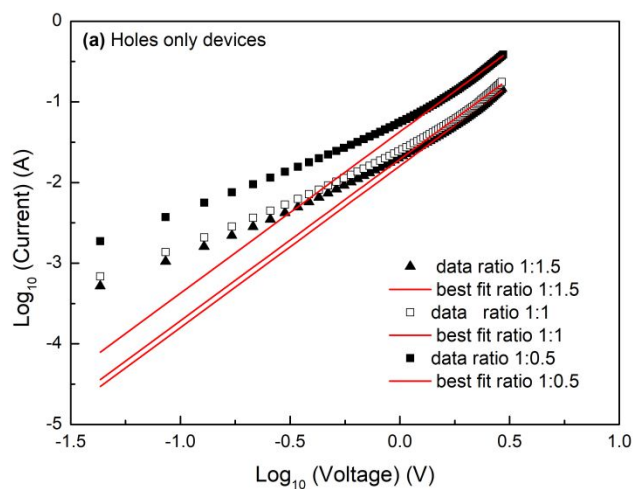


Figure 7. Current vs voltage for holes (a) and electron (b) only devices. The charges carrier mobilities of PTB7:PC₇₁BM blends were determined following the single-carrier devices SCLC model.

Table 2. Hole (μ_h) and electron (μ_e) mobility values obtained by SCLC of PTB7:PC₇₁BM bulk heterojunction layers without DIO as function of blend ratio.

| PTB7:PC ₇₁ BM ratio | Film | Average thickness d (nm) | μ_h (cm ² /V.s) | μ_e (cm ² /V.s) |
|--------------------------------|------|--------------------------|--------------------------------|--------------------------------|
| 1:1.5 | A | 73 | 3.9-4.3x10 ⁻⁴ | 5.88-6.15x10 ⁻⁴ |
| | B | 111 | 6.4-7.3x10 ⁻⁴ | 2.75-3.1x10 ⁻⁴ |
| 1:1 | C | 80 | 3.05-3.4x10 ⁻⁴ | 2.32-2.68x10 ⁻⁴ |
| | D | 119 | 0.97-1.23x10 ⁻³ | 0.95-1.15x10 ⁻⁴ |
| 1:0.5 | E | 50 | 7.23-7.77x10 ⁻⁴ | 3.86-5.45x10 ⁻⁶ |
| | F | 90 | 9.65-9.95x10 ⁻⁴ | 7.74-8.66x10 ⁻⁶ |

To understand fullerene aggregation and charge transport in the polymer phase, molecular dynamics simulations were adopted to estimate the enthalpy of mixing of the polymer:fullerene blends without DIO.²⁹ We previously reported that 50% of PC₇₁BM content generates a highly stable phase in which the blend and the separate phases have similar enthalpy values and thus no driving force for phase separation exists. The low mixing enthalpy derives from the high fullerene-PTB7 interaction that leads to densely packed regions of fullerene molecules (hereafter referred to as clusters) intercalated within the polymer. Figure 8a shows the fullerene organization inside the blend with 1:0.5, 1:1 and 1:1.5 weight ratio. We find that the fullerenes form clusters inside the polymer blend with a separation distance of less than ~1.5 Å. When decreasing the fullerene concentration from ratio of 1:1.5 down to 1:0.5, the size of the clusters decreases while their relative distance increases (see Figure 8a). In general, the key property for

1
2
3 the electron transport in the blend is the distance between fullerenes. The electron hopping is
4 efficient when the fullerene-fullerene distance (defined as the distance between fullerenes
5 surfaces) is comparable to the value of the crystalline PC₇₁BM phase, i.e. ~ 1.5 Å. As the distance
6 between fullerenes increases, the hopping probability decreases. Accordingly, the bottleneck for
7 electron mobility of the blends is the average distance \bar{d} between clusters. A cluster is here
8 defined as a group of fullerenes which are separated by less than ~ 1.5 Å. The calculated distance
9 $\bar{d}(x)$ increases when the fullerene concentration, $1:x$, decreases and we find values 4.27 Å, 5.89
10 Å and 7.76 Å for fullerene concentrations x equal to 1.5, 1 and 0.5, respectively. In order to
11 compare our results with the experimental mobilities, we assume that the electron mobility μ_e
12 decreases exponentially with cluster distance, i.e. $\mu_e(x) \sim C e^{-\bar{d}(x)/\delta}$, where C is unknown
13 constant and $\delta = 1.5$ Å. By using the values $\bar{d}(x)$ calculated in the atomistic models above it is
14 possible to fit C to reproduce the experimental mobilities of Table 2 (see Figure 8b). Error bars
15 are taken as the difference between the mobilities at the same polymer:fullerene weight ratio. At
16 $\bar{d} = 1.5$ Å, corresponding to the average distance between fullerenes in the bulk, we estimate a
17 mobility of $\mu_e = 2.85 \times 10^{-3}$ cm²/Vs, which is in the order of the experimental mobilities of neat
18 PC₇₁BM films.^{13,44,69} Our theoretical analysis shows that fullerenes are not homogeneously
19 distributed inside the PTB7 but tend to form elongated clusters along the backbone of the
20 polymer chains driven by the mixing enthalpy of the PTB7:PC₇₁BM blend. The average distance
21 between these nano-sized fullerene clusters governs the electron mobility. The nano-sized
22 fullerene clusters give rise to a network inside the polymer that favors electron transport towards
23 the fullerene-enriched domains.

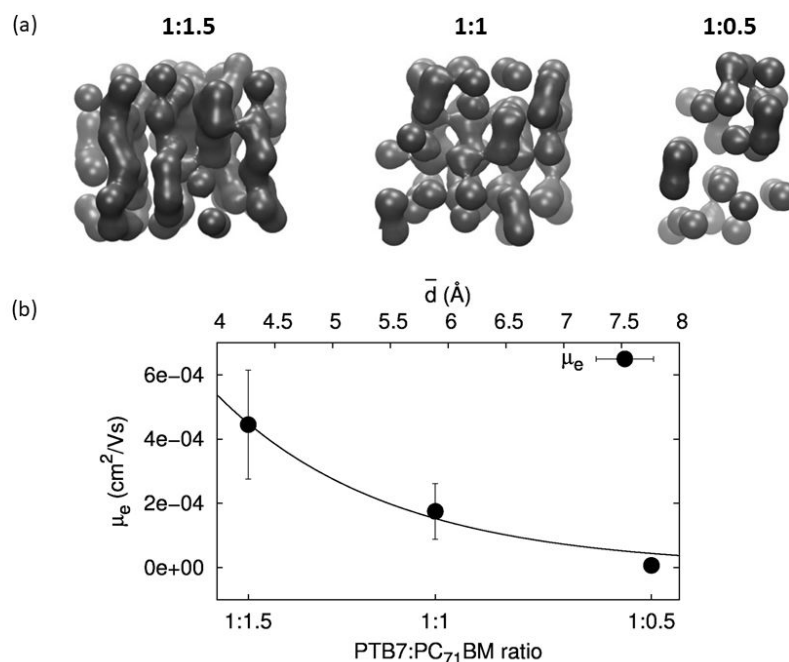


Figure 8. (a) Calculated PTB7:PC₇₁BM blend morphology as function of fullerene w% inside the polymer blend (shown on top of each panel). Only PC₇₁BM is shown for clarity. The models are built with identical amount of polymer and different fullerene concentrations. Grey iso-surfaces are obtained from a volumetric Gaussian density map (each fullerene is taken as single particle with coordinates equal to its center of mass) with radius scale equal to the average fullerene radius (i.e. ~ 3.7 Å), density isovalue equal to 0.5 Å, and grid spacing equal to 1 Å.^{55,58} (b) Experimental mobilities fitted by the model $\mu_e(x) \sim Ce^{-\bar{d}(x)/\delta}$, with $\delta = 1.5$ Å. We obtain $C = 7.74 \times 10^{-3}$ cm²/Vs.

4. CONCLUSION

Visualizing and analyzing the inner domain size distribution and absolute domain composition of fullerene-based polymer blend films is highly essential to correlate the morphology and the photocurrent generation. Here we studied PTB7:PC₇₁BM blend films processed without additive

1
2
3 via varying the ratio of PTB7 and PC₇₁BM in the active layer so that non-optimized blends were
4
5 created containing large fullerene domains or a single polymer enriched phase. Our results show
6
7 that fullerenes are not homogeneously distributed in the polymer phase but form clusters that, at
8
9 the higher fullerene concentrations, tend to form fullerene networks inside the donor phase.
10
11 Molecular dynamics simulations of the polymer-fullerene blends point towards the mixing
12
13 enthalpy of the PTB7:PC₇₁BM mixture as driving force for the cluster formation. The formation
14
15 of the fullerene network not only reduce the concentration of electron trap states but also
16
17 promote efficient electron transport paths inside the PTB7 phases via electron hopping processes.
18
19 The formation of the fullerene clusters is governed by the mixing enthalpy of the PTB7:PC₇₁BM
20
21 blend and depends thus on the chemical structure of both donor and acceptor materials. Our
22
23 future work will focus on the deeper understanding on the polymer:acceptor interaction so that a
24
25 voluntarily generation of an acceptor sub-networks in the polymer enriched domains is possible
26
27 by suitable design of non-fullerene acceptor. This can lead to enhanced electron extraction and
28
29 thus higher processing tolerance of high efficiency blends against formation of morphological
30
31 defects such as large polymer enriched domains surpassing the exciton diffusion lengths.
32
33
34
35
36
37
38
39
40

41 ASSOCIATED CONTENT

42 Supporting information

43
44 The supporting information is available free of charge on the ACS Publication website at
45
46 DOI:xxx.
47

48 Absorption spectra of PTB7, PC₇₁BM and a 1:1.5 blend films. 2D-GIXD patterns. 2D-GIXD
49
50 profiles (out of plane and in plane) of bare PTB7, PC₇₁BM and PTB7:PC₇₁BM blends. Electron
51
52 energy-loss spectra of pure PTB7 and PC₇₁BM. Annular dark-field images and fullerene
53
54 concentration maps using STEM-SI of the cross-sectional preparations of PTB7:PC₇₁BM blends
55
56 (ratio 1:1.5) processed with DIO and without DIO. Experimental average molecular fullerene
57
58 fractions in PTB7:PC₇₁BM blends of ratios 1:0.25, 1:0.5, 1:1, and 1:1.5 in comparison to
59
60 expected molecular fractions. High resolution annular dark-field image and fullerene
concentration map using STEM-SI of a PTB7:PC₇₁BM blend (ratio 1:0.5) processed without

DIO. Thickness values obtained by profilometry of PTB7:PC₇₁BM bulk heterojunction layers. Analysis of experimental mobilities by SCLC.

AUTHOR INFORMATION

Corresponding Authors

* E-mail: m.pfanmoller@uni-heidelberg.de (Martin Pfannmöller)

* E-mail: videlot@cinam.univ-mrs.fr (Christine Videlot-Ackermann)

ORCID

Sadok Ben Dkhil: [0000-0002-8035-7581](https://orcid.org/0000-0002-8035-7581)

Pavlo Perkhun: [0000-0001-7458-3411](https://orcid.org/0000-0001-7458-3411)

Sara Bals: [0000-0002-4249-8017](https://orcid.org/0000-0002-4249-8017)

Daiki Kuzuhara: [0000-0001-7948-8501](https://orcid.org/0000-0001-7948-8501)

Stephan Thierry Dubas: [0000-0002-7188-3096](https://orcid.org/0000-0002-7188-3096)

Claudia Caddeo: [0000-0002-1090-9897](https://orcid.org/0000-0002-1090-9897)

Alessandro Mattoni: [0000-0002-1381-6557](https://orcid.org/0000-0002-1381-6557)

Olivier Margeat: [0000-0003-3716-2399](https://orcid.org/0000-0003-3716-2399)

Uli Würfel: [0000-0003-4151-8538](https://orcid.org/0000-0003-4151-8538)

Jörg Ackermann: [0000-0003-2586-3788](https://orcid.org/0000-0003-2586-3788)

Martin Pfannmöller: [0000-0002-0910-1591](https://orcid.org/0000-0002-0910-1591)

Christine Videlot-Ackermann: [0000-0001-8240-6474](https://orcid.org/0000-0001-8240-6474)

Present Addresses

[§] Present address: Dracula Technologies, 4 Rue Georges Auric, 26000 Valence, France.

[#] Present address: Centre for Advanced Materials, Heidelberg University, 69120 Heidelberg, Germany.

Author Contributions

The manuscript was written through contributions of all authors. All authors have given approval to the final version of the manuscript.

Notes

The authors declare no competing financial interest.

ACKNOWLEDGMENTS

JA, OM and CVA acknowledge financial support by the French *Fond Unique Interministériel* (FUI) under the project “SFUMATO” (Grant number: F1110019V/201308815) as well as by the European Commission under the Project “SUNFLOWER” (FP7-ICT-2011-7, Grant number:

1
2
3 287594). JA, CVA and EB acknowledge the ANRT (Association Nationale de la Recherche et de
4 la Technologie) and the Ministère de l'Enseignement Supérieur, de la Recherche et de
5 l'Innovation, awarded through the company Dracula Technologies (Valence, France) for
6 framework of a CIFRE PhD grant 2017/0529. JA and PP received funding from the European
7 Union's Horizon 2020 research and innovation program under the Marie Skłodowska-Curie
8 Grant Agreement No. 713750. They further acknowledge support of the Regional Council of
9 Provence-Alpes-Côte d'Azur, A*MIDEX (No. ANR-11-IDEX-0001-02), and the
10 Investissements d'Avenir project funded by the French Government, managed by the French
11 National Research Agency (ANR). JA and YAAQ acknowledge the French Research Agency for
12 funding through the project NFA-15 (ANR-17-CE05-0020-01). NY acknowledges the
13 synchrotron radiation experiments were performed at BL19B2 in SPring-8 with the approval of
14 Japan Synchrotron Radiation Research Institute (JASRI) (Proposal Nos. 2017B1629 and
15 2018B1791). SB acknowledges financial support from the European Research Council (ERC
16 Consolidator Grant # 815128 -REALNANO) and from FWO (G.0381.16N). AM acknowledges
17 Italian MIUR for funding through the project PON04a2 00490 M2M Netergit, PRACE for
18 awarding access to Marconi KNL at CINECA, Italy, through projects DECONVOLVES
19 (2018184466) and PROVING-IL (2019204911). CC acknowledges the CINECA award under
20 the ISCRA initiative, for the availability of high performance computing resources and support
21 (project MITOMASC).

22 23 24 25 26 27 28 29 30 31 32 33 34 35 36 37 38 39 40 41 42 43 44 45 46 47 48 49 **REFERENCES**

- 50
51
52
53 (1) Li, G.; Zhu, R.; Yang, Y. Polymer Solar Cells. *Nat. Photonics* **2012**, *6*, 153-161.
54
55
56
57
58
59
60

- 1
2
3
4 (2) Li, H.; Xiao, Z.; Ding, L.; Wang, J. Thermostable Single-Junction Organic Solar
5 Cells with a Power Conversion Efficiency of 14.62%. *Sci. Bull.* **2018**, 63, 340–342.
6
7
8 (3) Inganäs, O. Organic Photovoltaics Over Three Decades. *Adv. Mater.* **2018**, 30,
9 1800388.
10
11
12 (4) Wadsworth, A.; Moser M.; Marks A.; Little M.S.; Gasparini N.; Brabec C.J.; Baran
13 D.; McCulloch I. Critical Review of the Molecular Design Progress in Non-Fullerene
14 Electron Acceptors Towards Commercially Viable Organic Solar Cells. *Chem. Soc. Rev.*
15 **2018**, 48, 1596–1625.
16
17
18 (5) Liu Q.; Jiang Y.; Jin K.; Qin J.; Xu J.; Li W.; Xiong J.; Liu J.; Xiao Z.; Sun K.;
19 Yang S.; Zhang X.; Ding L. 18% Efficiency Organic Solar Cells, *Science Bulletin* **2020**,
20 65, 272-275.
21
22
23 (6) Cui, Y. Yao H.; Hong L.; Zhang T.; Xu Y.; Xian K.; Gao B.; Qin J.; Zhang J.; Wei
24 Z.; Hou J. Achieving Over 15% Efficiency in Organic Photovoltaic Cells via Copolymer
25 Design. *Adv. Mater.* **2019**, 31, 1808356.
26
27
28 (7) Cui, Y.; Yao, H.; Zhang, J.; Zhang T.; Wang Y.; Hong L.; Xian K.; Xu B.; Zhang
29 S.; Peng J.; Wei Z.; Gao F.; Hou J. Over 16% Efficiency Organic Photovoltaic Cells
30 Enabled by a Chlorinated Acceptor with Increased Open-Circuit Voltages. *Nat.*
31 *Commun.* **2019**, 10, 2515.
32
33
34 (8) Ye L.; Hu H.; Ghasemi M.; Wang T.; Collins BA.; Kim J.H.; Jiang K.; Carpenter J.H.; Li
35 H.; Li Z.; McAfee T.; Zhao J.; Chen X.; Lai J.L.Y.; Ma T.; Brédas J.L.; Yan H.; Ade H.
36 Quantitative Relations between Interaction Parameter, Miscibility and Function in Organic Solar
37 Cells. *Nat. Mater.* **2018**, 17, 253-260.
38
39
40 (9) Fan, B.; Du X.; Liu F.; Zhong W.; Ying L.; Xie R.; Tang X.; An K.; Xin J.; Li N.; Ma
41 W.; Brabec C.J.; Huang F.; Cao Y. Fine-Tuning of the Chemical Structure of Photoactive
42 Materials for Highly Efficient Organic Photovoltaics. *Nat. Energy* **2018**, 3, 1051-1058.
43
44
45 (10) Menke, S. M., Ran, N. A., Bazan, G. C., Friend, R. H. Understanding Energy
46 Loss in Organic Solar Cells: Toward a New Efficiency Regime. *Joule* **2018**, 2, 25-35.
47
48
49
50
51
52
53
54
55
56
57
58
59
60

- 1
2
3
4 (11) Zhou, Z. Xu S.; Song J.; Jin Y.; Yue Q.; Qian Y.; Liu F.; Zhang F.; Zhu X. High-
5 Efficiency Small-Molecule Ternary Solar Cells with a Hierarchical Morphology Enabled
6 by Synergizing Fullerene and Non-Fullerene Acceptors. *Nat. Energy* **2018**, *3*, 952-959.
7
8
9 (12) Gao K.; Jo S.B.; Shi X.; Nian L.; Zhang M.; Kan Y.; Lin F.; Kan B.; Xu B.; Rong
10 Q.; Shui L.; Liu F.; Peng X.; Zhou G.; Cao Y.; Jen A. K.-Y. Over 12% Efficiency
11 Nonfullerene All-Small-Molecule Organic Solar Cells with Sequentially Evolved
12 Multilength Scale Morphologies. *Adv. Mater.* **2019**, *31*, 1807842.
13
14
15 (13) Liang, Y.; Xu, Z.; Xia, J.; Tsai, S. T.; Wu, Y.; Li, G.; Ray, C.; Yu, L. For the Bright
16 Future-Bulk Heterojunction Polymer Solar Cells with Power Conversion Efficiency of
17 7.4%. *Adv. Mater.* **2010**, *22*, 135–138.
18
19
20 (14) Brady M.A.; Su G.M.; Chabinyo M.L. Recent Progress in the Morphology of Bulk
21 Heterojunction Photovoltaics. *Soft Matter*. **2011**, *7*, 11065-11077.
22
23
24 (15) Hamed W.A.; Yahya R.; Bola A.L.; Ekramul Mahmud H.N.M. Recent
25 Approaches to Controlling the Nanoscale Morphology of Polymer-Based Bulk-
26 Heterojunction Solar Cells. *Energies* **2013**, *6*, 5847-5868.
27
28
29 (16) Xue R.; Zhang J.; Li Y.; Li Y. Organic Solar Cell Materials toward
30 Commercialization. *Small* **2018**, 1801793.
31
32
33 (17) Di Nuzzo, D.; Aguirre, A.; Shahid, M.; Gevaerts, V.S.; Meskers, S.C.J.; Janssen,
34 R.A.J. Improved Film Morphology Reduces Charge Carrier Recombination into the
35 Triplet Excited State in a Small Bandgap Polymer-Fullerene Photovoltaic Cell. *Adv.*
36 *Mater.* **2010**, *22*, 4321-4324.
37
38
39 (18) Collins B.A.; Li Z.; Tumbleston J.R.; Gann E.; McNeill C.R.; Ade H. Absolute
40 Measurement of Domain Composition and Nanoscale Size Distribution Explains
41 Performance in PTB7:PC₇₁BM Solar Cells. *Adv. Energy Mater.*, **2013**, *3*, 65-74.
42
43
44 (19) Min J.; Jiao X.; Ata I.; Osvet A.; Ameri T.; Bäuerle P.; Ade H.; Brabec C.J.
45 Time-Dependent Morphology Evolution of Solution-Processed Small Molecule Solar
46 Cells during Solvent Vapor Annealing. *Adv. Energy Mater.*, **2016**, *6*, 1502579.
47
48
49
50
51
52
53
54
55
56
57
58
59
60

- 1
2
3
4 (20) Wessendorf C.D.; Perez-Rodriguez A.; Hanisch J.; Arndt A. P.; Ata I.; Schulz
5 G.L.; Quintilla A.; Bäuerle P.; Lemmer U.; Wochner P.; Ahlswede E.; Barrena E.
6 Understanding the Effect of Solvent Vapor Annealing on Solution-Processed A–D–A
7 Oligothiophene Bulk-Heterojunction Solar Cells: The Role of Alkyl Side Chains. *J.*
8 *Mater. Chem. A*, **2016**, 4, 2571-2580.
- 9
10
11
12 (21) Hu, H.; Jiang, K.; Chow, P.C.Y.; Ye, L.; Zhang, G.; Li, Z.; Carpenter J.H.; Ade H.; Yan
13 H. Influence of Donor Polymer on the Molecular Ordering of Small Molecular Acceptors in
14 Nonfullerene Polymer Solar Cells. *Adv. Energy Mater.* **2017**, 8, 1701674.
- 15
16
17 (22) Zhu Y.; Gadisa A.; Peng Z.; Ghasemi M.; Ye L.; Xu Z.; Zhao S.; Ade H. Rational
18 Strategy to Stabilize an Unstable High-Efficiency Binary Nonfullerene Organic Solar
19 Cells with a Third Component. *Adv. Energy Mater.* **2019**, 9, 1900376.
- 20
21
22
23 (23) Song L.; Wang W.; Barabino E.; Yang D.; Körstgens V.; Zhang P.; Roth S. V.;
24 Müller-Burschbaum P. Composition–Morphology Correlation in PTB7-Th/PC₇₁BM Blend
25 Films for Organic Solar Cells. *ACS Appl. Mater. Interfaces* **2019**, 11, 3125-3135.
- 26
27
28
29 (24) Pfannmöller M.; Kowalsky W.; Schröder R.R. Visualizing Physical, Electronic,
30 and Optical Properties of Organic Photovoltaic Cells. *Energy & Environ. Sci.* **2013**, 6,
31 2871-2891.
- 32
33
34
35 (25) Pfannmöller M.; Flügge H.; Benner G.; Wacker I.; Sommer C.; Hanselmann M.;
36 Schmale S.; Schmidt H.; Hamprecht F.A.; Rabe T.; Kowalsky W.; Schröder R.R.
37 Visualizing a Homogeneous Blend in Bulk Heterojunction Polymer Solar Cells by
38 Analytical Electron Microscopy. *Nano Letters* **2011**, 11, 3099-3107.
- 39
40
41
42 (26) Wen J.; Miller D.J.; Chen W.; Xu T.; Yu L.; Darling S.B.; Zaluzec N.J.
43 Visualization of Hierarchical Nanodomains in Polymer/Fullerene Bulk Heterojunction
44 Solar Cells. *Microsc. Microanal.* **2014**, 20, 1507-1513.
- 45
46
47
48 (27) Moritomo, Y.; Yasuda, T.; Yonezawa, K.; Sakurai, T.; Takeichi, Y.; Suga H.;
49 Takahashi Y.; Inami, N.; Mase, K.; Ono, K. Fullerene Mixing Effect on Carrier Formation in
50 Bulk-Hetero Organic Solar Cell. *Sci. Rep.* **2015**, 5, 9483.
- 51
52
53
54
55
56
57
58
59
60

1
2
3
4 (28) Ben Dkhil, S.; Pfannmöller, M.; Schröder, R. R.; Alkarsifi, R.; Gaceur, M.;
5 Köntges, W.; Heidari, H.; Bals, S.; Margeat, O.; Ackermann, J.; Videlot-Ackermann C.
6 Interplay of Interfacial Layers and Blend Composition To Reduce Thermal Degradation
7 of Polymer Solar Cells at High Temperature. *ACS Appl. Mater. Interfaces* **2018**, 10,
8 3874– 3884.

9
10
11
12
13 (29) Ben Dkhil, S.; Pfannmöller, M.; Saba, M. I.; Gaceur, M.; Heidari, H.; Videlot-
14 Ackermann, C.; Margeat, O.; Guerrero, A.; Bisquert, J.; Garcia-Belmonte, G.; Mattoni A.;
15 Bals S.; Ackermann J. Toward High-Temperature Stability of PTB7-Based Bulk
16 Heterojunction Solar Cells: Impact of Fullerene Size and Solvent Additive. *Adv. Energy*
17 *Mater.* **2017**, 7, 1601486.

18
19
20
21
22 (30) Köntges, W.; Perkhun, P.; Kammerer, J.; Alkarsifi, R.; Würfel, U.; Margeat, O.;
23 Videlot-Ackermann, C.; Simon, J.-J.; Schröder, R.; Ackermann, J.; Pfannmöller, M.
24 Visualizing Morphological Principles for Efficient Photocurrent Generation in Organic
25 Non-fullerene Acceptor Blends. *Energy Environ. Sci.*, **2020**, 13, 1259-1268.

26
27
28
29
30 (31) He Z.; Zhong C.; Su S.; Xu M.; Wu H.; Cao Y. Enhanced Power-Conversion
31 Efficiency in Polymer Solar Cells Using an Inverted Device Structure. *Nat. Photon.*
32 **2012**, 6, 591-595.

33
34
35
36 (32) To C.H.; Ng A.; Dong Q.; Djurišić A. B.; Zapien J. A.; Chan W. K.; Surya C. Effect
37 of PTB7 Properties on the Performance of PTB7:PC₇₁BM Solar Cells. *ACS Appl. Mater.*
38 *Interfaces*, **2015**, 7, 13198-13207.

39
40
41
42 (33) Liu, C.; Wang, K.; Hu, X.; Yang, Y.; Hsu, C.-H.; Zhang, W.; Xiao, S.; Gong, X.;
43 Cao, Y. Molecular Weight Effect on the Efficiency of Polymer Solar Cells. *ACS Appl.*
44 *Mater. Interfaces* **2013**, 5, 12163-12167.

45
46
47
48 (34) Lou S. J.; Szarko J. M.; Xu T.; Yu L. P.; Marks T. J.; Chen L. X. Effects of
49 Additives on the Morphology of Solution Phase Aggregates Formed by Active Layer
50 Components of High-Efficiency Organic Solar Cells. *J. Am. Chem. Soc.* **2011**, 133,
51 20661-20663.

1
2
3
4 (35) Kim W.; Kim J. K.; Kim E.; Ahn T. K.; Wang D. H.; Park J. H. Conflicted Effects of
5 a Solvent Additive on PTB7:PC₇₁BM Bulk Heterojunction Solar Cells. *J. Phys. Chem. C*
6 **2015**, 119, 5954-5961.
7

8
9
10 (36) Wang L.; Zhao S. L.; Xu Z.; Zhao J.; Huang D.; Zhao L. Integrated Effects of Two
11 Additives on the Enhanced Performance of PTB7:PC₇₁BM Polymer Solar Cells.
12 *Materials* **2016**, 9, 171.
13

14
15
16 (37) Chen H.-Y.; Lin S. H.; Sun J.Y.; Hsu C.-H.; La S.; Lin C.-F. Morphologic
17 Improvement of the PBDTTT-C and PC₇₁BM Blend Film with Mixed Solvent for High-
18 Performance Inverted Polymer Solar Cells. *Nanotechnology* **2013**, 24, 484009.
19

20
21
22 (38) Alem S.; Chu T.; Tse S. C.; Wakim S.; Lu J.; Movileanu R.; Tao Y.; Bélanger F.;
23 Désilets D.; Beaupré S.; Leclerc M.; Rodman S.; Waller D.; Gaudiana R. Effect of Mixed
24 Solvents on PCDTBT:PC₇₀BM Based Solar Cells. *Org. Electron.* **2011**, 12, 1788-1793.
25

26
27
28 (39) Wang G. J.; Jiu T. G.; Tang G.; Li J.; Li P. D.; Song X. J.; Lu F. S.; Fang J. F.
29 Interface Modification of ZnO-Based Inverted PTB7:PC₇₁BM Organic Solar Cells by
30 Cesium Stearate and Simultaneous Enhancement of Device Parameters. *ACS*
31 *Sustainable Chem. Eng.* **2014**, 2, 1331-1337.
32
33

34
35
36 (40) Lu Y.; Xu T.; Jung I.H.; Yu L. Match the Interfacial Energy Levels Between Hole
37 transport Layer and Donor polymer to Achieve High Solar Cell performances. *J. Phys.*
38 *Chem. C* **2014**, 118, 22834-22839.
39

40
41
42 (41) Kniepert J.; Lange I.; Heidbrink J.; Kurpiers J.; Brenner T.J.K.; Koster L.J.A.;
43 Neher D. Effect of Solvent Additive on Generation, Recombination, and Extraction in
44 PTB7:PCBM Solar Cells: A Conclusive Experimental and Numerical Simulation Study.
45 *J. Phys. Chem. C* **2015**, 119, 8310-8320.
46
47

48
49
50 (42) Guerrero A.; Garcia-Belmonte G. Recent Advances to Understand Morphology
51 Stability of Organic Photovoltaics. *Nano-Micro Lett.* **2017**, 9:10.
52

53
54 (43) Guo, J. C.; Liang, Y. Y.; Szarko, J.; Lee, B.; Son, H. J.; Rolczynski, B. S.; Yu, L.
55 P.; Chen, L. X. Structure, Dynamics, and Power Conversion Efficiency Correlations in a
56
57

1
2
3
4 New Low Bandgap Polymer: PCBM Solar Cell. *J. Phys. Chem. B* **2010**, *114*, *2*, 742-
5 748.

6
7
8 (44) Ho C.H.Y.; Cheung S.H.; Li H.-W.; Chiu K.L.; Cheng Y.; Yin H.; Chan M.H.; So
9 F.; Tsang S.-W., So S.K. Using Ultralow Dosages of Electron Acceptor to Reveal the
10 Early Stage Donor–Acceptor Electronic Interactions in Bulk Heterojunction Blends. *Adv.*
11 *Energy Mater.* **2017**, 1602360.

12
13
14
15 (45) Dkhil, S. B.; Duché, D.; Gaceur, M.; Thakur, A. K.; Aboura, F.B.; Escoubas, L.;
16 Simon, J.-J.; Guerrero, A.; Bisquert, J.; Garcia-Belmonte, G.; Bao Q.; Fahlman M.;
17 Videlot-Ackermann C.; Margeat O.; Ackermann J. Interplay of Optical, Morphological,
18 and Electronic Effects of ZnO Optical Spacers in Highly Efficient Polymer Solar Cells.
19 *Adv. Energy Mater.* **2014**, *4*, 1400805.

20
21
22 (46) de la Peña F.; Prestat E.; Fauske V.T.; Burdet P.; Jokubauskas P.; Nord M.;
23 Garmannslund A.. (2019, September 6). hyperspy/hyperspy: HyperSpy v1.5.2 (Version v1.5.2).
24 Zenodo. <http://doi.org/10.5281/zenodo.3396791>.

25
26
27 (47) Newville M.; Otten R.; Nelson A.; Ingargiola A.; Stensitzki T.; Allan D.; Almarza A.
28 (2020, May 7). lmfitt/lmfitt-py 1.0.1 (Version 1.0.1). Zenodo.
29 <http://doi.org/10.5281/zenodo.3814709>.

30
31
32 (48) Blakesley J.C.; Castro F.; Kylberg W.; Dibb G. F.A.; Arantes C.; Valaski R.; Cremona
33 M.; Kim J. S.; Kim J.-S. Towards Reliable Charge-Mobility Benchmark Measurements for
34 Organic Semiconductors. *Org. Electronics* **2014**, *15*, 1263-1272.

35
36
37 (49) Wang J.; Wolf R.M.; Caldwell J.W.; Kollman P.A.; Case D.A. Development and
38 Testing of a General Amber Force Field. *J. Comput. Chem.* **2004**, *25*, 1157-1174.

39
40
41 (50) Mattioli, G.; Ben Dkhil, S.; Saba G.I.; Mallocci G.; Melis C.; Alippi P.; Filippone F.;
42 Thakur A.K.; Gaceur M.; Margeat O.; Diallo A.K.; Videlot-Ackermann C.; Ackermann J.;
43 Bonapasta A.A.; Mattoni A. Interfacial Engineering of P3HT/ZnO Hybrid Solar Cells Using
44 Phthalocyanines: A Joint Theoretical and Experimental Investigation. *Adv. Energy Mater.*
45 **2014**, *4*,1301694.

46
47
48 (51) Caddeo C.; Fazzi D.; Caironi M.; Mattoni A. Atomistic Simulations of P(NDI2OD-T2)
49 Morphologies: From Single Chain to Condensed Phases. *J. Phys. Chem. B* **2014**, *43*,
50 12556-12565.

- 1
2
3
4 (52) Caddeo C.; Dessì R.; Melis C.; Colombo L.; Mattoni A. Poly(3-hexylthiophene)
5 Adhesion on Zinc Oxide Nanoneedles. *J. Phys. Chem. C* **2011**, *115* (34), 16833-16837.
6
7
8 (53) Caddeo C.; Mattoni A. Atomistic Investigation of the Solubility of 3-Alkylthiophene
9 Polymers in Tetrahydrofuran Solvent. *Macromolecules* **2013**, *46* (19), 8003-8008.
10
11
12 (54) Phillips J.C.; Braun R.; Wang W.; Gumbart J.; Tajkhorshid E.; Villa E.; Chipot C.;
13 Skeel R.D.; Kalé L.; Schulten K. Scalable Molecular Dynamics with NAMD. *J. Comput.*
14 *Chem.* **2005**, *26*, 1781-802.
15
16
17 (55) Humphrey W.; Dalke A.; Schulten K. VMD: Visual Molecular Dynamics. *J. Mol.*
18 *Graphics* **1996**, *14*, 33-38.
19
20
21 (56) Bellani S.; Porro M.; Caddeo C.; Saba M.I.; Miranda P.B.; Mattoni A.; Lanzani G.;
22 Antognazza M.R. The Study of Polythiophene/Water Interfaces by Sum-Frequency
23 Generation Spectroscopy and Molecular Dynamics Simulations. *J. Mater. Chem. B*
24 **2015**, *3*, 6429-6438.
25
26
27 (57) Casalegno M.; Zanardi S.; Frigerio F.; Po R.; Carbonera C.; Marra G.; Nicolini T.; Raos
28 G.; Meille S.V. Solvent-Free Phenyl-C61-Butyric Acid Methyl Ester (PCBM) from
29 Clathrates: Insights for Organic Photovoltaics from Crystal Structures and Molecular
30 Dynamics. *Chem. Comm.* **2013**, *49*, 4525-4527.
31
32
33 (58) Krone M.; Stone J.E.; Ertl T.; Schulten K. Fast Visualization of Gaussian Density
34 Surfaces for Molecular Dynamics and Particle System Trajectories. *EuroVis - Short*
35 *Papers* **2012**, *1*, 67-71.
36
37
38 (59) Ebenhoch B.; Thomson S.A. J.; Genevičius K.; Juška G.; Samuel I.D.W. Charge
39 Carrier Mobility of the Organic Photovoltaic Materials PTB7 and PC₇₁BM and its
40 Influence on Device Performance. *Org. Electron.* **2015**, *22*, 62-68.
41
42
43 (60) Hammond M.R.; Kline J.; Herzing A.A.; Richter L.J.; Germack D.S.; Ro H.-W.;
44 Soles C.L.; Fischer D.A.; Xu T.; Yu L.; Toney M.F.; DeLongchamp D.M. Molecular
45 Order in High-Efficiency Polymer/Fullerene Bulk Heterojunction Solar Cells. *ACS Nano*
46 **2011**, *5*, 8248-8257.
47
48
49
50
51
52
53
54
55
56
57
58
59
60

- 1
2
3
4 (61) Guerrero A.; Pfannmoller M.; Kovalenko A.; Ripolles T.S.; Heidari H.; Bals S.;
5 Kaufmann L.-D.; Bisquert J.; Garcia-Belmonte G. Nanoscale Mapping by Electron
6 Energy-Loss Spectroscopy Reveals Evolution of Organic Solar Cell Contact Selectivity.
7 *Org. Electron.* **2015**, *16*, 227-233.
8
9
10
11 (62) Lou S.J.; Szarko J.M.; Xu T.; Yu L.P.; Marks T.J.; Chen L.X. Effects of Additives
12 on the Morphology of Solution Phase Aggregates Formed by Active Layer Components
13 of High-Efficiency Organic Solar Cells. *J. Am. Chem. Soc.* **2011**, *133*, 20661-20663.
14
15
16
17 (63) Chen W.; Xu T.; He F.; Wang W.; Wang C.; Strzalka J.; Liu Y.; Wen J.; Miller
18 D.J.; Chen J.; Hong K.L.; Yu L.; Darling S.B. Hierarchical Nanomorphologies Promote
19 Exciton Dissociation in Polymer/Fullerene Bulk Heterojunction Solar Cells. *Nano Lett.*
20 **2011**, *11*, 3707-3713.
21
22
23
24
25 (64) Deibel C.; Dyakonov V.; Brabec C.J. Organic Bulk-Heterojunction Solar Cells.
26 *IEEE J. Sel. Top. Quantum Electron.* **2010**, *16*, 1517-1527.
27
28
29
30 (65) Shaw, P. E.; Ruseckas, A.; Samuel, I. D. W. Exciton Diffusion Measurements in
31 Poly(3-hexylthiophene). *Adv. Mater.* **2008**, *20*, 3516-3520.
32
33
34 (66) Foster S.; Deledalle F.; Mitani A.; Kimura T.; Kim K.-B.; Okachi T.; Kirchartz T.;
35 Oguma J.; Miyake K.; Durrant J.R.; Doi S.; Nelson J. Electron Collection as a Limit to
36 Polymer:PCBM Solar Cell Efficiency: Effect of Blend Microstructure on Carrier Mobility
37 and Device Performance in PTB7:PCBM. *Adv. Energy Mater.* **2014**, *4*, 1400311.
38
39
40
41 (67) Zhou N.; Lin H.; Lou S.J.; Yu X.; Guo P.; Manley E.F.; Loser S.; Hartnett P.;
42 Huang H.; Wasielewski M.R.; Chen L.X.; Chang R.P.H.; Facchetti A.; Marks T.J.
43 Morphology-Performance Relationships in High-Efficiency All-Polymer Solar Cells. *Adv.*
44 *Energy Mater.* **2014**, *4*, 1300785.
45
46
47
48
49 (68) Uy R.L.; Price S.C.; You W. Structure–Property Optimizations in Donor Polymers
50 via Electronics, Substituents, and Side Chains toward High Efficiency Solar Cells.
51 *Macromol. Rapid Commun.* **2012**, *33*, 1162-1177.
52
53
54
55
56
57
58
59
60

1
2
3
4 (69) Ho C.H.Y.; Dong Q.; Yin H.; Leung W.W.K.; Yang Q.; Lee H.K.H.; Tsang S.W.;
5 So S.K. Impact of Solvent Additive on Carrier Transport in Polymer:Fullerene Bulk
6 Heterojunction Photovoltaic Cells. *Adv. Mater. Interfaces* **2015**, 2, 1500166.
7
8
9
10
11
12
13
14
15
16
17
18
19
20
21
22
23
24
25
26
27
28
29
30
31
32
33
34
35
36
37
38
39
40
41
42
43
44
45
46
47
48
49
50
51
52
53
54
55
56
57
58
59
60

Graphical abstract

